Journal of ELECTRONIC MATERIALS
DOI: 10.1007/s11664-008-0435-2

Power Generator Modules of Segmented Bi_2Te_3 and ErAs:$(InGaAs)_{1-x}(InAlAs)_x$

GEHONG ZENG,[1,7] JE-HYEONG BAHK,[1] JOHN E. BOWERS,[1] HONG LU,[2] JOSHUA M.O. ZIDE,[3] ARTHUR C. GOSSARD,[2] RAJEEV SINGH,[4] ZHIXI BIAN,[4] ALI SHAKOURI,[4] SUZANNE L. SINGER,[5] WOOCHUL KIM,[6] and ARUN MAJUMDAR[5]

1.—Department of Electrical and Computer Engineering, University of California, Santa Barbara, CA 93106, USA. 2.—Materials Department, University of California, Santa Barbara, CA 93106, USA. 3.—Electrical and Computer Engineering Department, University of Delaware, Newark, DE 19716, USA. 4.—Electrical Engineering Department, University of California, Santa Cruz, CA 95064, USA. 5.—Department of Mechanical Engineering, University of California, Berkeley, CA 94720, USA. 6.—School of Mechanical Engineering, Yonsei University, Seoul 120-749, Korea. 7.—e-mail: gehong@ece.ucsb.edu

The thermoelectric properties of ErAs:InGaAlAs were characterized by variable-temperature measurements of thermal conductivity, electrical conductivity, and Seebeck coefficient from 300 K to 600 K, which shows that the $ZT(=\alpha^2\sigma T/\kappa$, where α, σ, κ, and T are the Seebeck coefficient, electrical conductivity, thermal conductivity, and absolute temperature, respectively) of the material is greater than 1 at 600 K. Power generator modules of segmented elements of 300 μm Bi_2Te_3 and 50 μm thickness ErAs:$(InGaAs)_{1-x}(InAlAs)_x$ were fabricated and characterized. The segmented element is 1 mm × 1 mm in area, and each segment can work at different temperature ranges. An output power up to 5.5 W and an open-circuit voltage over 10 V were measured. Theoretical calculations were carried out and the results indicate that the performance of the thermoelectric generator modules can be improved further by improving the thermoelectric properties of the element material, and reducing the electrical and thermal parasitic losses.

Key words: ErAs, nanoparticle, solid-state generator, thermoelectrics

INTRODUCTION

Solid-state thermoelectric power generators are interesting sources of power because of their long life, robustness, compact size, light weight, and high reliability. Applications range from waste heat recovery in land and sea vehicles to deep-space exploration.[1] The output power and efficiency of a thermoelectric generator module depends largely on the material's thermoelectric properties, which are often summarized with the figure of merit ZT. Thermoelectric properties can be improved by introducing nanometer scale structure into materials. In this way, the power factor ($\alpha^2\sigma$) can be enhanced because of the quantum confinement effect[2]; thermal conductivity can be reduced due to the increase of phonon interface scattering[3–9]; and the Seebeck coefficient can be increased through energy filtering.[10–13] Reduction of the thermal conductivity using superlattice heterostructures or incorporation of nanoparticles has been demonstrated.[9,14,15] The Seebeck coefficient and electrical conductivity for most materials are inversely related with each other: the Seebeck coefficient will decrease when the electrical conductivity rises. In our study, ErAs nanoparticles, a rocksalt semimetal nanostructure, were epitaxially incorporated into $(InGaAs)_{1-x}(InAlAs)_x$ using molecular beam epitaxy (MBE). The ErAs nanoparticles in the InGaAlAs can provide

(Received December 6, 2007; accepted February 26, 2008)

charge carriers, and serve as electron filtering and phonon scattering centers. Theoretical studies show that the ErAs nanoparticles form effective phonon scattering centers for middle- and long-wavelength phonons, which explains the reduction of thermal conductivity.[16] The combination of a large Seebeck coefficient, low thermal conductivity, and possibly high electrical conductivity can dramatically improve the material's figure of merit ZT.

Low output voltage and low output power have been problems for thermoelectric generators. Solid-state generator modules with output power in watts and output voltage in volts are needed in most real applications and this drove our research into a solid-state generator module using ErAs:$(InGaAs)_{1-x}$ $(InAlAs)_x$ elements. In our previous research, 400 element generator modules were fabricated using ErAs nanoparticles embedded in InGaAs/InAlAs superlattice layers 5 μm thick. The element area size was 200 μm $\times$ 200 μm, and an output power per module around 7 mW was measured.[17] The performance was mainly limited by the small temperature drop across the elements, large electrical parasitic loss, and low electrical conductivity of the p-type InGaAs/InAlAs superlattice.

In this article, we report recent advances in new ErAs:$(InGaAs)_{1-x}(InAlAs)_x$ alloy material and the fabrication and characterization of 254 segmented element generator modules of 300 μm thickness Bi_2Te_3 and 50 μm thickness ErAs:$(InGaAs)_{1-x}$ $(InAlAs)_x$. An output power of 5.5 W and an open circuit voltage over 10 V were measured when the heat source temperature was around 600 K.

MATERIAL CHARACTERIZATION

The ErAs:$(InGaAs)_{1-x}(InAlAs)_x$ samples were grown using a Varian Gen III molecular beam epitaxy system on lattice-matched (100) InP substrates.[18–20] The growth rate was about 2 μm per hour and the growth temperature was maintained at 490°C. The n-type ErAs:$(InGaAs)_{1-x}(InAlAs)_x$ consists of 80% InGaAs and 20%InAlAs, while the p-type sample is ErAs:InGaAs. The erbium arsenide concentration in both samples is 0.3% by volume. Both n-type and p-type samples have a 1 μm cap layer and a 250 nm buffer layer, which are doped InGaAs layers. The doping levels were designed to be 9×10^{18} cm^{-3} and 5×10^{19} cm^{-3} for n-type and p-type samples, respectively. The doped cap and buffer layers were used as contact layers for low metallization contact resistance.

The role of incorporating ErAs nanoparticles is to reduce the thermal conductivity below that of the InGaAs or InGaAlAs alloy. It has been shown that incorporating ErAs nanoparticles 1 nm to 5 nm in diameter effectively reduces the thermal conductivity below that of InGaAs because ErAs nanoparticles effectively scatter long- and middle-wavelength phonons while atomic substitution in InGaAs alloy scatters short-wavelength phonons.[16]

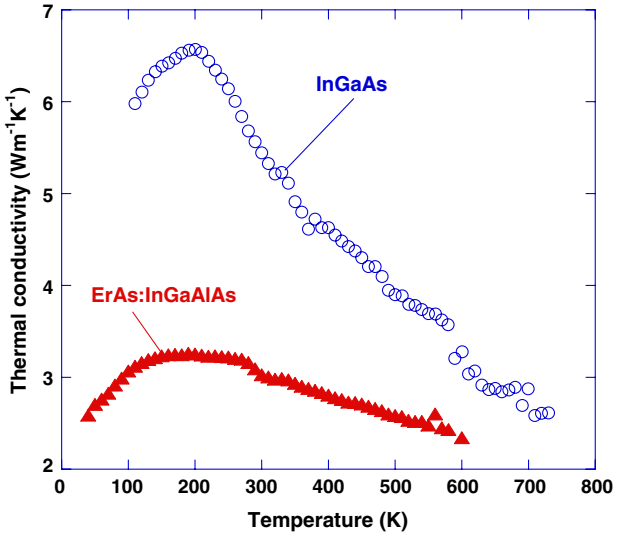

Fig. 1. The measurement result of thermal conductivity for ErAs:InGaAlAs (the values of InGaAs used for comparison) using the 3ω method.

The thermal conductivity of $(InGaAs)_{0.8}(InAlAs)_{0.2}$ with 0.3% ErAs nanoparticles was measured using the 3ω method as shown in Fig. 1.

Since the Seebeck coefficient and electrical conductivity are inversely related for most materials, the enhancement of the Seebeck coefficient usually reduces the electrical conductivity. Therefore, there is an optimum carrier concentration where the maximum value of $\alpha^2\sigma$ occurs. However, in this system, it is possible to increase the electrical conductivity and Seebeck coefficient simultaneously. When ErAs nanoparticles are incorporated into $(InGaAs)_{1-x}(InAlAs)_x$, potential barriers are formed at the interface between the particle and semiconductor. This barrier height varies with temperature and can be adjusted by varying the InAlAs concentration, which can be optimized to act as an energy barrier for charge carriers. The Seebeck coefficient can therefore be enhanced through the electron filtering effects of these potential barriers.[21]

In order to measure the Seebeck coefficient and electrical conductivity, n-type samples with epitaxial layers of 0.3% ErAs:$(InGaAs)_{0.8}(InAlAs)_{0.2}$ with 0.5 μm and 2 μm thickness, respectively, were grown on semi-insulating InP substrates about 520 μm thick. The 2 μm epitaxial layer samples were processed for Seebeck coefficient measurements. The test chips were cut into 5×20 mm^2 in strip size, and coated with 300 nm Si_3N_4 on both the top and bottom sides. The contact electrodes of Ni/GeAu metallization and barrier metal layers were made at each end of the strip chip. The test setup consists of two copper bars embedded with heaters placed in a vacuum chamber, and the test sample was placed across the two separated bars, which were set at different temperatures. The temperature difference ΔT and output voltage V were measured directly and the Seebeck coefficient α was the slope of the linearly

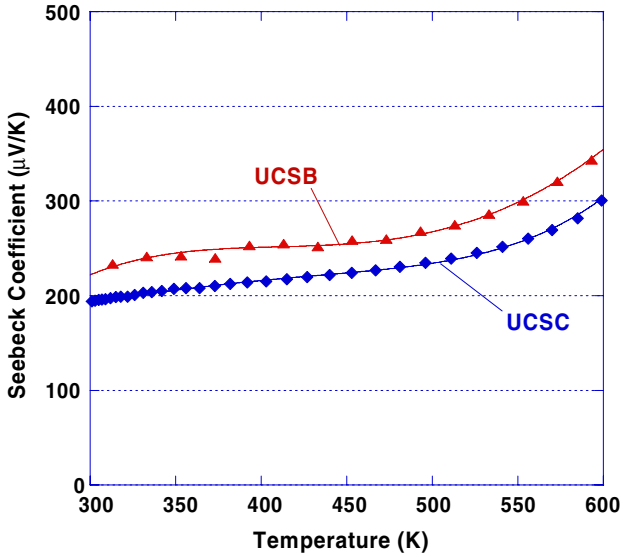

Fig. 2. Seebeck coefficients of *n*-type $(InGaAs)_{0.8}(InAlAs)_{0.2}$ with 0.3% ErAs nanoparticles versus temperature from 300 K to 600 K.

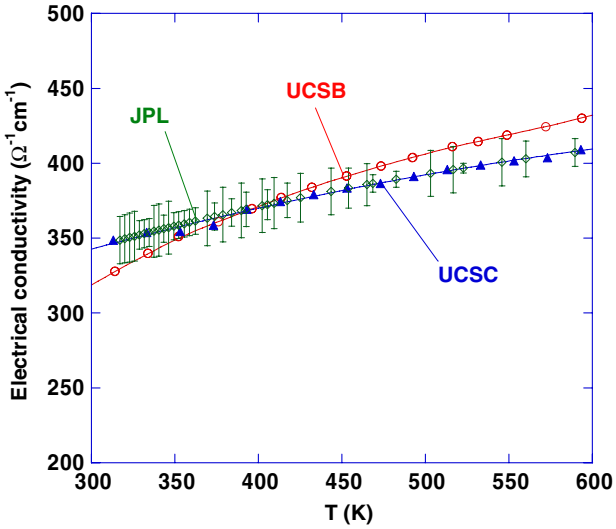

Fig. 3. The electrical conductivity of *n*-type $(InGaAs)_{0.8}(InAlAs)_{0.2}$ with 0.3% ErAs nanoparticles measured at JPL, UCSC, and UCSB, respectively.

fitted V versus ΔT, which is expressed as $\alpha = V/\Delta T$. Different Seebeck coefficient test samples from the same material wafer were measured separately at both University of California at Santa Barbara (UCSB) and University of California at Santa Cruz (UCSC) to ensure that measurements were carried out properly. The results from the two groups showed similar values and trends of Seebeck coefficients versus temperatures from 300 K to 600 K, as shown in Fig. 2.

Epitaxial layer samples 0.5 μm thick were used for van der Pauw measurements. The test samples were cut into 1 cm × 1 cm square chips. The sample was coated with 300 nm Si_3N_4 as a protection layer to prevent oxidation or diffusion of the material at high temperatures. Four contact metal electrodes of contact metallization of Ni/GeAu and barrier metal layers were deposited on the four corners. The measurements were carried out in a vacuum of around 1×10^{-3} Torr. The test chips from the same wafer samples were measured at UCSB, UCSC, and the Jet Propulsion Laboratory (JPL). The measurement results of electrical conductivity from 300 K to 600 K are shown in Fig. 3. As the electrical conductivity of the semi-insulating InP substrate will substantially increase with temperature, the Seebeck coefficient and electrical conductivity of the InP substrate must be taken into account. To get a better understanding of the side effects of the substrate, the electrical conductivity of the semi-insulating InP substrate was measured from 300 K to 600 K, and the values are $1.2 \times 10^{-4}\ \Omega^{-1}\,cm^{-1}$, $6.4 \times 10^{-4}\ \Omega^{-1}\,cm^{-1}$, $2.7 \times 10^{-3}\ \Omega^{-1}\,cm^{-1}$, and $2 \times 10^{-2}\ \Omega^{-1}\,cm^{-1}$ at 300 K, 400 K, 500 K, and 600 K, respectively. The electrical conductivity difference between the ErAs:InGaAlAs epitaxial layer and InP substrate is reduced from six orders of magnitude to four orders of magnitude, and effects from the InP substrate are expected to be significant when the temperature is above 600 K. These side effects of the substrate can be totally extinguished by removing the InP substrate. The variable-temperature measurements of ErAs:InGaAlAs epitaxial layers without InP substrate are underway.

An *n*-type ErAs:InGaAlAs sample 20 μm thick was grown on a semi-insulating InP substrate and measured at room temperature to find the difference of the electrical conductivity and Seebeck coefficient between the in-plane and cross-plane directions. The in-plane properties were measured using van der Pauw and bar-shaped patterns for electrical conductivity and Seebeck coefficient measurements, respectively, while the cross-plane properties were measured via transient methods using device test patterns of different sizes. The results show that the electrical conductivity is 348 $\Omega^{-1}cm^{-1}$ and 374 $\Omega^{-1}cm^{-1}$, and the Seebeck coefficient is 224 μV/K and 241 μV/K for in-plane and cross-plane, respectively, which indicates that the difference between the in-plane and cross-plane properties of the material is not significant.

The Seebeck coefficients of InGaAs or InGaAlAs are usually less than 100 μV/K at room temperature with doping around 1×10^{19} cm^{-3}. By incorporating ErAs nanoparticles, the cross-plane Seebeck coefficient of ErAs:InGaAlAs was measured to be 241 μV/K at room temperature. This value is very close to 235 μV/K, the cross-plane Seebeck coefficient of ErAs:InGaAs/InGaAlAs superlattice at the same doping,[10] which indicates that the potential barrier around ErAs nanoparticles has similar electron filter effects as that of superlattices. Based on the measurements of thermal conductivity, electrical conductivity, and Seebeck coefficient, the figure of merit of *n*-type ErAs:InGaAlAs is shown in Fig. 4 with the ZT value of 0.16 at 300 K, and 1 at 600 K.

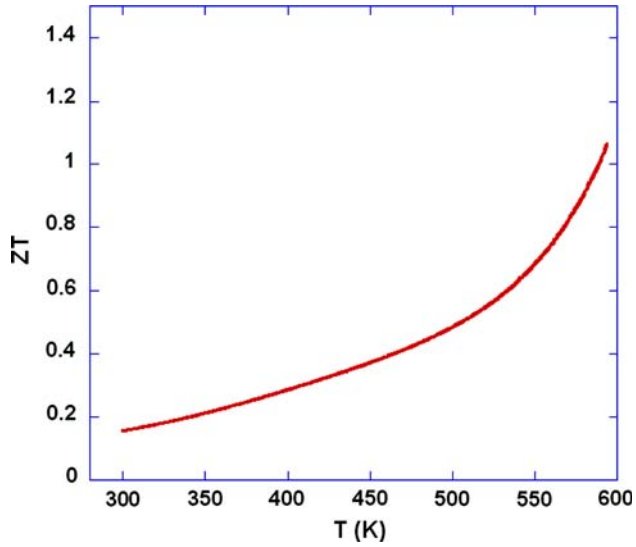

Fig. 4. The ZT values of n-type $(InGaAs)_{0.8}(InAlAs)_{0.2}$ with 0.3% ErAs nanoparticles based on the measurements on the thermal conductivity, electrical conductivity, and Seebeck coefficients from temperatures of 300 K to 600 K.

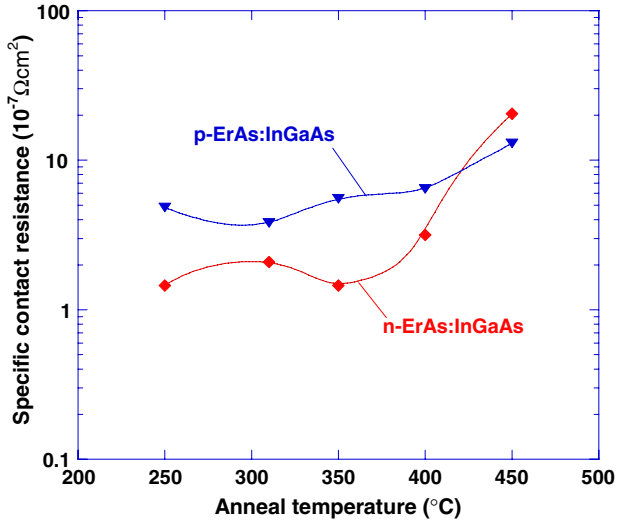

Fig. 5. Specific contact resistance measurements for n-ErAs: InGaAs and p-ErAs:InGaAs using the TLM.

DEVICE FABRICATION

The segmented generator modules were fabricated via the pick-and-place approach and flip-chip bonding techniques. Processing techniques similar to those of standard large-scale integrated circuits were used for the fabrication of the segmented elements of ErAs:InGaAlAs and Bi_2Te_3.

MBE was used to grow epitaxial layers on two 75 mm InP wafers: one n-type 50 μm ErAs: $(InGaAs)_{0.8}(InAlAs)_{0.2}$ wafer and one p-type 50 μm ErAs:InGaAs wafer.

The thin-film element fabrication started with the front-side metallization of the epitaxial layer; Ni/GeAu/Ni/Au contact metals were used for n-type ErAs:InGaAlAs and Pt/Ti/Pt/Au were used for p-type ErAs:InGaAs. The InP substrate was removed using wet etching solution to expose the backside of the epitaxial layer. The backside metallization was similar to that of the front side: Ni/GeAu/Ni/Au and Pt/Ti/Pt/Au were used for n-type and p-type, respectively. Then the n- and p-type thin-film wafers were diced into square chips ready for bonding.

Two of the key factors in obtaining low contact resistance are the surface structure conditions and cleanliness. The normal surface preparation before contact metal deposition is to use oxygen plasma to remove organic residues on the surface, and then the surface oxide is removed by wet etching in HF or HCl solutions. It is believed that some micron sized structures may be produced on the surface under energetic bombardment during oxygen plasma treatment, which may increase the contact resistance. This is especially true for ohmic contacts to p-type materials, where the contact resistance is sensitive to surface structure conditions.[22] Studies show that the organic or nonorganic residues on the surface can be effectively cleaned, and the stoichiometric composition at the surface can be maintained in ultraviolet ozone treatment.[23]

The surface oxide film of InGaAs or InP-based materials is removed in HF or HCl solutions, but the surface will oxidize after being exposed to air. In our experiments, ammonia solutions were used for surface oxide film cleaning. After ammonia solution treatment, the sample surfaces will still be in an ammonia environment while the samples are mounted and the vacuum chamber is pumped down. Ammonia is volatile, and can be easily pumped out of the chamber. Thus, clean surfaces were achieved, which was important for low resistance contacts.

Transmission-line method (TLM) patterns were fabricated for the specific contact resistance measurements. Figure 5 shows the TLM measurement results for both n and p ErAs:InGaAs materials, and the specific contact resistances for both types were on the order of 10^{-7} Ω cm^2.

Ni was used as the contact metallization for Bi_2Te_3 of both n- and p-type. After metallization, the bulk Bi_2Te_3 was cut into square chips of 1 mm $\times$ 1 mm in area. All the Bi_2Te_3 elements were bonded on a lower ceramic plate, while the ErAs: InGaAlAs elements were bonded on an upper ceramic plate. Finally, the lower Bi_2Te_3 bonded plate and the upper ErAs:InGaAlAs bonded plate were bonded together using AuSn solder via flip-chip bonding to form a 254-element generator module.

MEASUREMENT RESULTS AND DISCUSSIONS

The schematic diagram of the generator module is shown in Fig. 6. The measurement setup for generator modules consists of a heat sink with water cooling, a heat source consisting of two cartridge heaters, thermocouples for temperature monitoring, and

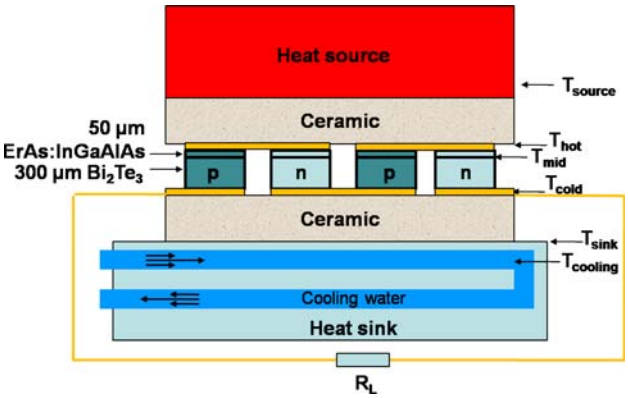

Fig. 6. Schematic diagram of the segmented element power generator.

electrical probes. Two thermocouples were used for temperature measurements: one of the thermocouples was on the top of the generator for the measurement of the heat source temperature; the other was placed on top of the heat sink at the edge of the generator's lower ceramic plate. The output current flowing through the power generator and the output voltage generated across an external electrical resistor load were measured. The data acquisition was done via four multimeters controlled by a computer.

The dependence of the output power and open-circuit voltage on the hot-side temperature is shown in Figs. 7 and 8, respectively. During the measurements, the temperature rise measured at the edge of the generator cold plate was less than 5 K. The output power was measured in impedance-matched condition (300 K) with a constant external resistor of 4.7 Ω. When the heat source temperature rises above 500 K, the output power gradually shows some saturation. To get a better understanding of

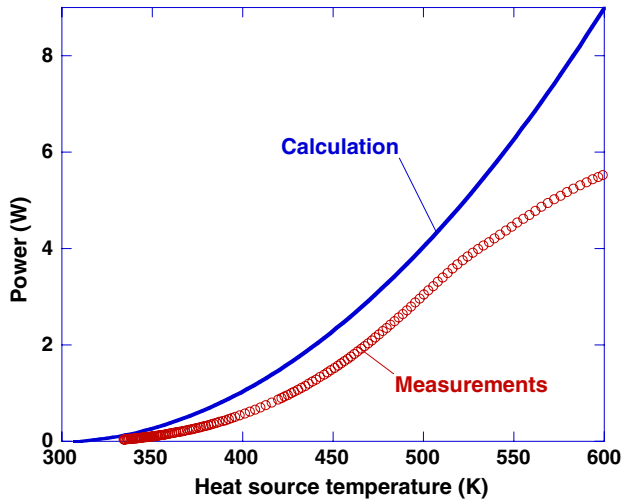

Fig. 7. The output power measurement results for the power generator module of 254 segment elements of 50 μm ErAs:$(InGaAs)_{1-x}$ $(InAlAs)_x$ and 300 μm Bi_2Te_3 with cooling water temperature at 285 K. Also shown is the calculated power output from this module.

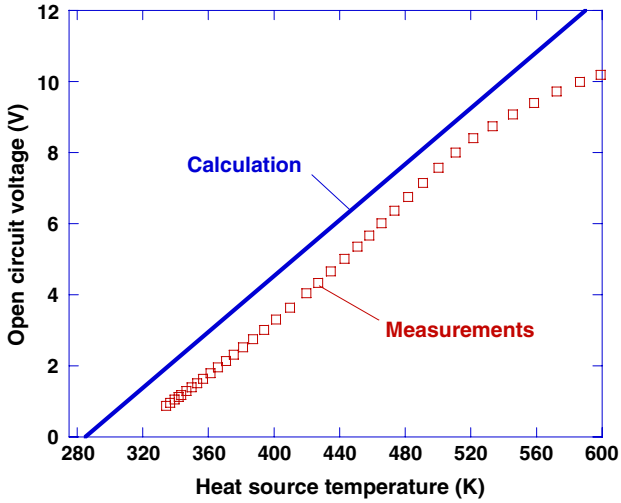

Fig. 8. The measurement results of open circuit voltage for the power generator module of 254 segment elements of 50 μm ErAs:$(InGaAs)_{1-x}(InAlAs)_x$ and 300 μm Bi_2Te_3 with cooling water temperature at 285 K. Also shown is the calculated open-circuit voltage from this module.

the performance of generator modules, theoretical calculations were carried out. The combined thermal conductance K, the electrical resistance r, and the Seebeck coefficient α for a p–n element couple can be given as:

$$K = \frac{\kappa_p S_p}{l_p} + \frac{\kappa_n S_n}{l_n} \tag{1}$$

$$r = \frac{\rho_p l_p}{S_p} + \frac{\rho_n l_n}{S_n} \tag{2}$$

$$\alpha = \alpha_n - \alpha_p, \tag{3}$$

where κ, ρ, S, and l are the thermal conductivity, electrical resistivity, element size, and element thickness for n- or p-type elements, respectively. In adiabatic conditions, the heat flows from the heat source through the segmented element array to the heat sink, finally being carried away by the cooling water (Fig. 6) and can be described using Eqs. 4–7, respectively:

$$\begin{aligned} &\frac{1}{R_{\text{ceramic}}} \cdot (T_{\text{source}} - T_{\text{hot}}) \\ &\quad = K_{\text{ErAs}} \cdot (T_{\text{hot}} - T_{\text{mid}}) + \alpha_{\text{ErAs}} \cdot I \cdot T_{\text{hot}} \\ &\quad\quad - \frac{1}{2} \cdot (r_{\text{ErAs}} + r_{\text{parasitic\_ErAs}}) \cdot I^2 \end{aligned} \tag{4}$$

$$\begin{aligned} &K_{\text{ErAs}} \cdot (T_{\text{hot}} - T_{\text{mid}}) + \alpha_{\text{ErAs}} \cdot I \cdot T_{\text{mid}} \\ &\quad + \frac{1}{2} \cdot (r_{\text{ErAs}} + r_{\text{parasitic\_ErAs}}) \cdot I^2 \\ &\quad = K_{\text{BiTe}} \cdot (T_{\text{mid}} - T_{\text{cold}}) + \alpha_{\text{BiTe}} \cdot I \cdot T_{\text{mid}} \\ &\quad\quad - \frac{1}{2} \cdot (r_{\text{BiTe}} + r_{\text{parasitic\_BiTe}}) \cdot I^2 \end{aligned} \tag{5}$$

$$K_{\mathrm{BiTe}} \cdot (T_{\mathrm{mid}} - T_{\mathrm{cold}}) + \alpha_{\mathrm{BiTe}} \cdot I \cdot T_{\mathrm{cold}} + \frac{1}{2} \cdot (r_{\mathrm{BiTe}} + r_{\mathrm{parasitic\_BiTe}}) \cdot I^2 = \frac{1}{R_{\mathrm{ceramic}}} (T_{\mathrm{cold}} - T_{\mathrm{sink}}) \quad (6)$$

$$\frac{1}{R_{\mathrm{ceramic}}} (T_{\mathrm{cold}} - T_{\mathrm{sink}}) = h \cdot S_{\mathrm{ceramic}} \cdot (T_{\mathrm{sink}} - T_{\mathrm{cooling}}) \quad (7)$$

where I is the electrical current, h is the heat transfer coefficient of the heat sink, $r_{\mathrm{parasitic}}$ is the combined parasitic resistance of ohmic contact and connection metal pad resistance to each n–p element couple, and $R_{\mathrm{ceramic}} = L_{\mathrm{ceramic}}/\kappa_{\mathrm{ceramic}} \cdot S_{\mathrm{ceramic}}$ is the thermal resistance of the ceramic plates, where L_{ceramic}, $\kappa_{\mathrm{ceramic}}$, and S_{ceramic} are the thickness, thermal conductivity, and size of the ceramic plate, respectively. In our generator modules, there exists the heat constriction from heat source to elements through the upper ceramic plate, and the heat spreading from elements to the heat sink through the lower ceramic plate. Based on a theoretical model refined by Seri Lee,[24] the thermal resistance of the ceramic plates can be expressed as

$$R_{\mathrm{ceramic}} = \frac{L_{\mathrm{ceramic}}}{\kappa_{\mathrm{ceramic}} \cdot S_{\mathrm{ceramic}}} + \frac{1}{2 \cdot \kappa_{\mathrm{ceramic}} \sqrt{S_{\mathrm{ceramic}}}} \times \left(1 - \sqrt{\frac{S_{\mathrm{element}}}{S_{\mathrm{ceramic}}}}\right)^{\frac{3}{2}} \times \frac{\tanh(L_{\mathrm{ceramic}} \cdot \delta) + \frac{\kappa_{\mathrm{ceramic}} \cdot \delta}{h}}{1 + \frac{\kappa_{\mathrm{ceramic}} \cdot \delta}{h} \tanh(L_{\mathrm{ceramic}} \cdot \delta)}, \quad (8)$$

where $\delta = \sqrt{\pi^3/S_{\mathrm{ceramic}}} + \sqrt{1/S_{\mathrm{element}}}$, h is the heat transfer coefficient, S_{element} is the element size, and S_{ceramic} is the ceramic plate area size per element. The ratio, $S_{\mathrm{element}}/S_{\mathrm{ceramic}}$, is the fill factor of a generator module.

The calculation results of output power and open circuit voltage are compared with the measurement results in Figs. 7 and 8. The measurement results are lower than the calculated values through all temperature ranges. When the heat source temperature is below 500 K, the difference between the theoretical values and real device measurements indicates that there are some parasitic losses, which could be thermal and/or electrical. When the heat source temperature is above 500 K, the difference between the calculation and the measurements becomes larger, and the power versus heat-source temperature response gradually becomes saturated. There are two reasons for this: (i) the ZT value of Bi_2Te_3 drops at higher temperatures and (ii) the temperature at the cold side of the generator module also begins to rise due to the high heat flux through the elements, so that the temperature difference across the element does not increase linearly with increasing heat-source temperature. The difference between the calculated values and real device measurements of the open-circuit voltage indicates that there are some thermal parasitic losses between the heat source and the generator module, and between the generator module and the heat sink. The decrease of the Seebeck coefficient of the bulk Bi_2Te_3 when the heat-source temperature is over 500 K also causes the open-circuit voltage to become saturated (Fig. 8).

The performance of the generator modules can be improved by improving the thermoelectric properties of the elements, reducing the thermal and electrical parasitic loss, and increasing the heat transfer coefficient of the heat sink, which will effectively increase the temperature difference across the elements.

CONCLUSIONS

The incorporation of ErAs nanoparticles into $(InGaAs)_{1-x}(InAlAs)_x$ alloy results in significant improvements in the material's thermoelectric properties. Variable temperature measurements show that the ZT value reaches 1 at around 600 K, which is very encouraging. Segmented generator modules were fabricated using ErAs:InGaAlAs and Bi_2Te_3. Output power up to 5.5 W and open-circuit voltage of 10 V were measured with a heat-source temperature of around 600 K. The performance of thermoelectric generator modules can be further improved by improving the material thermoelectric properties, reducing electrical and thermal parasitic resistance loss, and improving the heat transfer coefficient of the heat sink.

ACKNOWLEDGEMENTS

The authors are grateful to Dr. Thierry Caillat at Jet Propulsion Laboratory for the variable temperature measurements of the electrical conductivities of ErAs:$(InGaAs)_{1-x}(InAlAs)_x$ samples. We also acknowledge useful discussions with Dr. Mihal Gross. This work is supported by the Office of Naval Research Thermionic Energy Conversion Center MURI, and ONR Contract N00014-05-1-0611.

REFERENCES

1. D.M. Rowe, *Thermoelectrics Handbook Macro to Nano* (New York: CRC, 2005).
2. L.D. Hicks and M.S. Dresselhaus, *Phys. Rev. B* 47, 16631 (1993). doi:10.1103/PhysRevB.47.16631.
3. M.V. Simkin and G.D. Mahan, *Phys. Rev. Lett.* 84, 927 (2000), Medline. doi:10.1103/PhysRevLett.84.927.
4. J.C. Caylor, K. Coonley, J. Stuart, T. Colpitts, and R. Venkatasubramanian, *Appl. Phys. Lett.* 87, 023105 (2005). doi:10.1063/1.1992662.
5. C. Dames and G. Chen, *J. Appl. Phys.* 95, 682 (2004). doi:10.1063/1.1631734.
6. T.C. Harman, P.J. Taylor, D.L. Spears, and M.P. Walsh, *J. Electron. Mater.* 29, L1 (2000). doi:10.1007/s11664-000-0117-1.
7. T.C. Harman, M.P. Walsh, B.E. Laforge, and G.W. Turner, *J. Electron. Mater.* 34, L19 (2005). doi:10.1007/s11664-005-0083-8.
8. T.P. Hogan, A. Downey, J. Short, J. D'Angelo, C.I. Wu, E. Quarez, J. Androulakis, P.F.P. Poudeu, J.R. Sootsman, D.Y. Chung, M.G. Kanatzidis, S.D. Mahanti, E.J. Timm,

H. Schock, F. Ren, J. Johnson, and E.D. Case, *J. Electron. Mater.* 36, 704 (2007). doi:10.1007/s11664-007-0174-9.
9. R. Venkatasubramanian, E. Siivola, T. Colpitts, and B. O'Quinn, *Nature* 413, 597 (2001), Medline. doi:10.1038/35098012.
10. G. Zeng, J.M.O. Zide, W Kim, J.E. Bowers, A.C. Gossard, Z. Bian, Y. Zhang, A. Shakouri, S.L. Singer, and A. Majumdar, *J. Appl. Phys.* 101, 034502 (2007). doi:10.1063/1.2433751.
11. A. Shakouri and J.E. Bowers, *Appl. Phys. Lett.* 71, 1234 (1997). doi:10.1063/1.119861.
12. D. Vashaee and A. Shakouri, *Phys. Rev. Lett.* 92, 106103/1 (2004).
13. D. Vashaee and A. Shakouri, *J. Appl. Phys.* 95, 1233 (2004). doi:10.1063/1.1635992.
14. S.T. Huxtable, A.R. Abramson, C.L. Tien, A. Majumdar, C. LaBounty, X. Fan, G. Zeng, J.E. Bowers, A. Shakouri, and E.T. Croke, *Appl. Phys. Lett.* 80, 1737 (2002). doi:10.1063/1.1455693.
15. W. Kim, S.L. Singer, A. Majumdar, D. Vashaee, Z. Bian, A. Shakouri, G. Zeng, J.E. Bowers, J.M.O. Zide, and A.C. Gossard, *Appl. Phys. Lett.* 88, 242107 (2006). doi:10.1063/1.2207829.
16. W. Kim, J. Zide, A. Gossard, D. Klenov, S. Stemmer, A. Shakouri, and A. Majumdar, *Phys. Rev. Lett.* 96, 045901 (2006), Medline. doi:10.1103/PhysRevLett.96.045901.
17. G. Zeng, J.E. Bowers, J.M.O. Zide, A.C. Gossard, W. Kim, S. Singer, A. Majumdar, R. Singh, Z. Bian, Y. Zhang, and A. Shakouri, *Appl. Phys. Lett.* 88, 113502 (2006). doi:10.1063/1.2186387.
18. D.C. Driscoll, M. Hanson, C. Kadow, and A.C. Gossard, *Appl. Phys. Lett.* 78, 1703 (2001). doi:10.1063/1.1355988.
19. D.C. Driscoll, M.P. Hanson, E. Mueller, and A.C. Gossard, *J. Crystal Growth* 251, 243 (2003). doi:10.1016/S0022-0248(02)02511-3.
20. J.M. Zide, D.O. Klenov, S. Stemmer, A.C. Gossard, G. Zeng, J.E. Bowers, D. Vashaee, and A. Shakouri, *Appl. Phys. Lett.* 87, 112102 (2005). doi:10.1063/1.2043241.
21. J.M.O. Zide, D. Vashaee, Z.X. Bian, G. Zeng, J.E. Bowers, A. Shakouri, and A.C. Gossard, *Phys. Rev. B* 74, 205335 (2006). doi:10.1103/PhysRevB.74.205335.
22. Z.M. Griffith (Ph.D. thesis, University of California, Santa Barbara, 2005).
23. R. Driad, W.R. McKinnon, Z.H. Lu, and S.P. McAlister, *J. Electr. Mater.* 29, L33–L36 (2000). doi:10.1007/s11664-000-0127-z.
24. S. Lee, S. Song, V. Au, and K.P. Moran, in *ASME/JSME Thermal Engineering Conference*, vol. 4 (1995), pp. 199–206.